Check for updates

Immune-theranostic gold nanorod-based NIR-responsive nanomedicine for the delivery of TLR7/8 adjuvant-induced effective anticancer therapy

Karunanidhi Gowsalya,[a] Babu Rithisa,[b] Selvaraj Shyamsivappan[b] and Raju Vivek ⓘ *[a]

Presently, there are several challenges that need to be overcome in the development of treatments that can effectively inhibit tumor growth, prevent the spread of tumor metastases, and protect the host against recurrence. Accordingly, a powerful synergistic immunotherapy method was developed to achieve the treatment of cancer. Herein, we established an improvement in the nanoengineering of gold nanorod (GNR)-mediated photothermal therapy (PTT) with theranostic indocyanine green (ICG), which also produced heat for effective PTT under near-infrared (NIR) light. Furthermore, co-encapsulated resiquimod (R848) induced the activation of an immune response against the tumor. In addition, a nuclear-targeted transactivator of transcription (TAT) peptide conjugated with FA-functionalized GNRs was produced for intranuclear tumor-targeted *in vivo* photothermal therapeutic efficacy, inducing DAMPs for immunogenic cell death (ICD). Post-PTT release of R848-activated TLR7/8 is essential for the development of a potent antitumor immune response by increasing the number of T cells, which recognize and kill tumors. Thus, this integrated immunotherapy method can be utilized for both the diagnosis and treatment of tumor recurrence, providing novel opportunities for both basic and clinical research. Collectively, our findings suggest that nanotechnology may be a useful technique for improving the efficacy of vaccine-based cancer immunotherapy.

1. Introduction

Cancer has a very high rate of mortality worldwide. According to estimations by the United Nations, cancer will cause 13.2 million deaths worldwide by 2030.[1] Cervical cancer ranks third among the most frequently diagnosed cancers in women and is the leading cause of cancer-related fatalities. Hence, there is an urgent need for novel approaches to diagnose and treat cancer, focusing on early detection treatment, minimizing the side effects of drugs, and enhancing the effectiveness of anticancer therapies.[2,3] Clinical treatment is characterized by treatments such as surgery, chemotherapy, and radiation therapy.[4] Unfortunately, these approaches cause damage to the body, such as the death of normal tissues, compromising the immune system, and an increase in tumor invasion.[5] Furthermore, cancer cells develop resistance to therapy quickly, rendering many treatments ineffective.[6,7] Surgery is

often used as the first line of defense for eliminating primary tumors, but it is invasive and may increase the risk of contracting secondary tumors, whereas radiation and immunotherapy may harm the immune system.[4,8] Thus, researchers have been focused on enhancing the efficacy and safety issues associated with current therapeutic procedures because of the complexity of cancer and the risks associated with traditional therapies.[9,10]

In this case, the strategies applied include making use of the enhanced permeability and retention (EPR) effect of nanomaterials, integrating tumor-targeting ligands, and modifying the tumor microenvironment (TME).[11] One such method, known as photothermal therapy (PTT), is the selective heating of tissue using electromagnetic radiation (such as visible light, infrared light, near-infrared light (NIR), radio waves, and microwaves) to kill cancer cells through light-to-heat conversion.[12] NIR light-sensitive gold nanorods (GNRs) have received significant attention as a potential cancer treatment in recent years. It has been shown that cancer cells can be killed by hyperthermia brought on by NIR laser-mediated photothermal ablation, whereas surrounding healthy tissues are unharmed.[13,14] Optical absorption in biological tissues may be seen in two different NIR spectral ranges of 650–900 nm (NIR-I

[a]Bio-Nano Theranostic Research Laboratory, Cancer Research Program (CRP), School of Life Sciences, Bharathiar University, Coimbatore-641 046, TN, India. E-mail: vivekr@buc.edu.in

[b]Department of Chemistry, Dr. N.G.P. Arts and Science College, Coimbatore-641048, TN, India

window) and 1000–1200 nm (NIR-II window).[15] NIR laser-mediated photothermal ablation has been found to cause little collateral damage to healthy tissues.[16,17] The tumor-ablating properties of GNR are attributed to the efficient enhancement in their unique optical and electronic features by photothermal conversion in cancer therapy.[18,19] It has also been shown that the half-life of GNR ($t_{1/2}$ = 17 h) in terms of photothermal heat generation and blood circulation is much longer than that of gold nanoshells ($t_{1/2}$ = 3 to 4 h). The seed-mediated strategy has been shown to be one of the most effective methods for the synthesis of GNR thus far.[20,21] However, GNR have several serious drawbacks, such as high biotoxicity, scattering loss, and poor photothermal stability.[22] NIR-light has deep tissue penetration, combined with efficient absorption in the NIR region of GNR, making them ideal for bio-applications. Due to the shape deformation (also known as the 'melting effect') during laser irradiation, the unique localized surface plasmon resonance (LSPR) properties of bare GNR are quickly lost, reducing both the PA signal and the photothermal efficiency.[13] Recently, the use of nanoparticles (NPs) in nuclear-targeted therapeutics was explored. The nuclear matrix has been shown to be the most heat-sensitive organelle in cells. Hence, creating a unique nuclear targeting material for targeted PTT at the cost of NIR requires high photothermal conversion efficiency (PCE), intranuclear accumulation, strong biocompatibility, and easy production.[7,23] However, the development of NPs with the selectivity required to penetrate the nuclear envelope and cytoplasmic membrane is a significant challenge. Nuclear pore complexes (NPCs) are 70 nm in size and protect the nuclear envelope, in addition to allowing materials to pass freely between the cytoplasm and the nucleoplasm.[24] In this case, the TAT peptide is a well-established nuclear localization signal (NLS) peptide that may be used to gain entry into the nucleus of cancer cells and cause significant cell damage.[25]

Most importantly, indocyanine green (ICG) is a theranostic photothermal agent and an amphiphilic tricarbocyanine dye that dissolves in water.[26] Being a negatively charged cyanine, it possesses capability for the strong absorption of NIR light. In 1958, the US FDA approved ICG as safe for diagnostic usage. Furthermore, ICG is quickly flushed from the body given that its half-life is very short (approximately 2 to 4 min).[26,27] The molecular weight of ICG is about 774.96 g mol^{-1}, and its hydrodynamic diameter is 1.2 nm.[28] Immunogenic cell death (ICD) modalities are promising given that they not only kill cancer cells directly but also stimulate the immune system to fight a broad range of solid tumors.[29] By producing an immunogenic "hot" cancer microenvironment, these vaccine-like approaches have the potential to increase the effectiveness of immunotherapies and improve outcomes by changing a "cold" TME.[30] ICD results in the generation of damage-associated molecular patterns (DAMPs) and tumor-associated antigens (TAAs), which are then gathered by dendritic cells (DCs) and macrophages for processing and presentation to adaptive immune cells.[14] Calreticulin (CRT), adenosine triphosphate (ATP), high mobility group box 1 (HMGB-1), and heat shock

proteins (HSPs) are examples of DAMPs.[18] TNF-α, IL-6, and IL-12 might all play a role in the significant inflammation that results after ICD release.[31] By increasing the invasion of immune effectors cells, we may change an immunosuppressive TME into an immunogenic TME, which may enhance the response rates to immune adjuvants and checkpoint blockade immunotherapy.[32,33] However, despite these advantages, photothermal immunotherapy may have adverse effects, such as lower doses at which the immune system becomes overactive due to the systemic infusion of therapeutic drugs.[34] In addition to eradicating tumors, the ideal cancer therapy will also activate the immune system to seek, locate, and destroy any remaining cancer cells. In this case, Resiquimod (R848) has the potential to increase the rate of cytokine production.[35] By stimulating the production of a variety of immunomodulatory cytokines, R848 both stimulates antigen-presenting cells (APCs) and internalizes T-cell responses. The importance of toll-like receptors (TLRs) in anticancer immune surveillance has increased in recent years; however, they were originally studied for their ability to trigger innate immune responses.[36,37] TLR7/8 activation is critical for the development of an efficient antitumor immune response because it increases the number of CD8$^+$ T cells, which recognize tumor antigens.[38] The FDA has approved R848 for local use in cancer therapy, which increases cytokine production and activates macrophages.[39] The development of carrier systems for the co-administration of immunotherapy and PTT has been prompted by the need to improve outcomes.[40] In this case, a significant hurdle is the rapid clearance of immune-activating small molecules such as R848 before they can reach their site of action. Thus, it is necessary to develop better delivery systems for a more focused and sustained immune response,[41] improving the effectiveness and safety of these immune-activating drugs. The only safe place for R848 to be released is within immune cells, and thus an efficient delivery mechanism must direct it there first.[42]

As mentioned above, considering the advantages of photothermal immunotherapy, NIR-controlled drug release and targeted delivery of therapeutic platforms, the effective prevention of recurrence can be realized.[43] Scheme 1 depicts the localized photothermal immunotherapy platform we created for the treatment of cancer and its prevention. The well-designed nanocomposite (NC) incorporates two important components for the efficient killing and prevention of tumors. NC is formed by the self-assembly method with ICG, R848, nuclear-targeting ligand TAT peptide and tumor-specific ligand FA. R848 is a TLR7/8 agonist, which means that it stimulates DCs to create inflammatory cytokines by binding to and activating several TLRs. When combined with TAAs generated locally during PTT of residual tumors, the NIR laser irradiation of NC-induced high temperature triggers the on-demand release of R848 and serves as a vaccination. To treat tumors with a combination of PTT and immunotherapy, we modified nuclear-targeted GNRs with TAT and loaded the R848 immunoadjuvant. The improved NC has potential to kill tumor cells directly via NIR-induced PTT and elicit an efficient immune response with
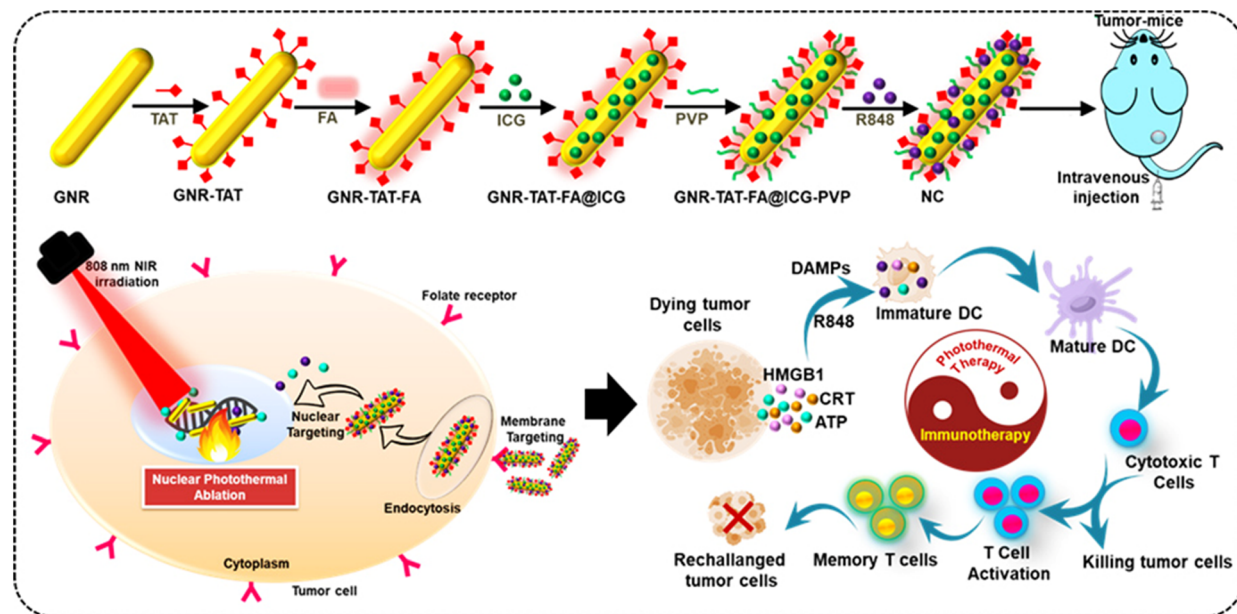
Scheme 1 Schematic representation of the process for the synthesis of NC. Primarily, NC enters tumor cells *via* membrane targeting (FA) and then enters the nucleus through nuclear targeting (TAT), finally reaching the nucleus without FA and TAT ligands. ICG and R848 releases are employed for further photothermal immunotherapy. Furthermore, the dying cells from the tumor site can activate the ICD markers and induce the levels of HMGB1, ATP, and CRT. In addition, R848 administration in tumor sites can enhance the activation of immune molecule functions from irradiated tumor cells. NIR-induced R848 release for TLR 7/8 activation, which is accompanied by the release of immunogenic factors associated with tumors that are presented to T cells.

the help of the loaded immunoadjuvant in both *in vitro* and *in vivo* situations due to its outstanding biocompatibility and photothermal stability. Thus, the NIR-irradiated NC not only inhibited the progression of cancer but also induced a strong, long-lasting immune memory against tumor recurrence.

2. Experimental

2.1. Materials

Tetrachloroauric acid trihydrate 99.5% ($HAuCl_4 \cdot 3H_2O$), cetyltrimethylammonium bromide (CTAB), ascorbic acid, silver nitrate ($AgNO_3$), sodium borohydride ($NaBH_4$), indocyanine green (ICG), folic acid (FA), Dulbecco's modified Eagle's medium (DMEM), phosphate-buffered saline (PBS), fetal bovine serum (FBS), and 3-(4,5-dimethyl thiazolyl-2)-2,5-diphenyltetrazolium bromide (MTT) were commercially obtained. Hi-Media Laboratories Pvt. Ltd (Mumbai) and Sigma-Aldrich Chemicals Pvt. Ltd (India) supplied all the chemicals used in the experiment. Peptides with the TAT sequence GRKKRRQRRRPQ were purified to 96% using GenScript. The all cell lines used in this study were procured from the National Centre for Cell Science (NCCS), India. In our experiments, we employed double-distilled water as the solvent.

2.2. Preparation of GNR

The preparation of GNR was performed according to the previous method.[25] The mentioned study described a two-step process for the synthesis of GNR. In summary, the reduction

of $HAuCl_4$ to create gold seeds was accelerated by using ice-cold $NaBH_4$ and CTAB. Subsequently, the slow development of gold seeds was facilitated by $HAuCl_4$ solutions containing $AgNO_3$, CTAB, and L-ascorbic acid. After being centrifuged at 8000 rpm for 30 min, the product was redistributed in ddH_2O.

2.3. Modification of GNR with TAT peptide

10 μL of 10 μM TAT peptide was mixed with 40 μL of GNR solution in a molecular ratio of 30 : 1 and incubated at 30 °C for 12 h. The GNR-TAT complex was centrifuged twice at 8000 rpm for 10 min to separate it from the free TAT. 50 μL of double-distilled water was used to resuspend the precipitate.[44]

2.4. Synthesis of FA conjugated GNR-TAT

The FA-modified GNR-TAT nanoconjugate was synthesized according to the previously reported method.[45] After rapidly stirring 5 mL aqueous GNR solution at 80 °C for about 2 h, 10 mL of FA-modified GNR-TAT was obtained. After cooling to room temperature, FA (150 mg in 5 mL ethanol) was sonicated for 10 min using an ultrasonic probe. PVP was used in the reported research to stabilize GNR. We diluted some PVP in water (about 1% by weight) and stored it. Then 1 mL of GNR-TAT-FA/ICG dissolved in water was added to 10 mL of PVP solution. The solution became a brownish-green color, indicating the formation of GNR-TAT-FA/ICG-PVP. For 7 min at 1500 rpm, the resulting cold solution was centrifuged to separate the solids. The collected precipitate was discarded. For

further study, we refrigerated the clear supernatant containing the purified GNR-TAT-FA/ICG-PVP at 7–10 °C.

2.5. Loading capacity and loading efficiency of ICG

With the help of a simple incubation technique, the LC of ICG was determined.[46] In this method, we used a shaker to incubate 1 mg of GNR-TAT-FA with 1 mL of ICG solution for 24 h. After centrifugation, the NPs coated with ICG were collected and washed three times in distilled water. The supernatant ICG concentration was calculated using a calibration curve and UV-visible spectra in the absorbance region of 780 nm. The ICG loading in the physically modified GNR-TAT-FA was reduced to 10% by evaporation. Overnight, 9 mL of GNR-TAT-FA was continually mixed with 1 mL of ICG ethanol solution. The solvent was evaporated at a temperature of 40 °C using a rotary evaporator. The round-bottom flask containing GNR-TAT-FA was properly dried and filled with ICG. The ICG loading capacity and loading efficiency were calculated using the following equations:

$$\text{LC of ICG }(\%) = \frac{\text{Weight (drug)}}{\text{Weight (drug)} + \text{Weight (Particles)}} \times 100$$

$$\text{LC of ICG }(\%) = \frac{128\,\mu\text{g}}{128 + 872\,\mu\text{g}} \times 100 = 12.8\%$$

(a)

$$\text{LE of ICG }(\%) = \frac{\text{Mass (drug loaded onto the particles)}}{\text{Mass (Initial drug added from stock)}} \times 100$$

$$\text{LE of ICG }(\%) = \frac{71.8\,\mu\text{g}}{100\,\mu\text{g}} \times 100 = 71.8\%$$

(b)

2.6. Loading capacity and loading efficiency of R848

According to the reported procedure, the R848 loading and release ratio were determined.[47] To load R848, 100 µL of an R848 methanol solution containing 10 mg mL^{-1} was added to 900 µL of a suspension of GNR-ICG, and the combination was stirred for 12 h. After centrifugation, the solution that was separated from the supernatant was collected and stored for further examination. The following equations were used to calculate the loading capacity and loading efficiency of R848

$$\text{LC }(\%) = (\text{mass of loaded R848/mass of NC}) \times 100$$

$$\text{EE }(\%) = (\text{mass of loaded R848/mass of fed R848}) \times 100$$

2.7. Instrumentation

The GNR sample was placed on copper grids for examination by transmission electron microscopy (TEM). The TEM images were analyzed using an 80 kV JEOL JEM 1400 Plus microscope. Electron-dispersive X-ray spectroscopy (EDX) was performed to evaluate the elements present in the samples employing a Thermo Fisher Talos 200X at 200 kV. The EDX maps were created using software from Thermo Scientific. We used a Malvern Instrument Zetasizer ZS 90 to measure the hydrodynamic diameter and zeta potential of the samples after diluting

100 µL of sample with 900 µL of distilled water. Absorption spectra were recorded in the ultraviolet, visible, and near-infrared (UV-vis-NIR) range for each sample. We recorded the UV-visible absorbance spectra in the range of 450 to 950 nm using a device made in India by TestRight Nanosystems Pvt. Ltd. A mixture of a very small amount of sample and KBr powder was investigated by Fourier transform infrared spectroscopy using a Thermo Nicolet FTIR Avatar 370. Using an X-ray diffractometer (Diffrac Plus v1.01) set to a Cu anode, 40 kV, 30 mA, 2 scales, and a wavelength of 1.54, the composition of NC was determined.

2.8. The photothermal efficiency of the NC

We quantitatively evaluated the photothermal performance of NC by exposing 25, 50, 75, and 100 µg mL^{-1} aqueous solutions of NC to an NIR laser at 1 W cm^{-2} for 5 min, while continually measuring the temperature. The thermal images were taken using a Testo-875 infrared thermal imager from Germany. To examine the photothermal stability of NC, five ON/OFF cycles at 1 W cm^{-2} for 5 min each were performed on the aqueous solution. We measured the PCE (η) of NC to demonstrate its photothermal conversion capability. A solution of NC was illuminated with an NIR 808 nm laser at a power density of 1 W cm^{-2} to evaluate when it reached a constant temperature (within 5 min). Then, the laser was turned off, and the solution was allowed to gradually cool to room temperature. According to the method reported by Roper, the η value was calculated[48] as follows:

$$\eta = \frac{hA\Delta T_{\max} - Q_{\text{s}}}{I(1 - 10 - A_{\lambda})}$$

where h is the heat transfer coefficient, A is the cross-sectional area of the container, Q_{s} is the heat associated with the light absorbance of the solvent, I is the laser power, A_{λ} is the absorbance of NC at 808 nm, and $\Delta T_{\max}$ is the highest temperature change. The η value of NC was calculated to be 40.31%. This high η value indicated that NC is a promising and suitable photothermal agent to generate sufficient hyperthermia to kill cancer cells.

2.9. ICG release from NC

After dispersing NC in PBS (1 mL, pH = 7.4) or an acetic acid sodium acetate buffer (1 mL, pH = 5.0), the kinetics of ICG release was examined by dialyzing 1 mg of ICG-loaded NC against 9 mL of the corresponding buffer media. In a vapor bathing vibrator, the release systems were warmed to 37 °C, maintained in the dark, and vibrated at 100 rpm per min. Subsequently, 1 mL of the buffer medium was extracted from the release mechanism at different periods to measure the quantity of released ICG using UV-vis spectroscopy at a wavelength of 808 nm. By continually introducing the same concentration of buffer solution, the outer phase buffer medium could be maintained at a constant concentration. Three total iterations of this process were performed.

2.10. R848 release from NC

Hermetically sealed dialysis bags (MWCO = 10 000) were filled with NC that had been suspended in 9 mL of PBS or acetate buffer. The whole apparatus was kept at a steady 37 °C temperature in a vapor bath vibrator. 1 mL of the buffer fluid was taken out at regular intervals and analyzed using UV-Vis spectroscopy. By adding 1 mL of the buffer solution, the volume of the outer phase buffer was kept constant.

2.11. Cell culture

Traditional methods for culturing HeLa cells included feeding them DMEM with 10% heat-inactivated FBS and 1% antibiotic solution. A humidified atmosphere with 5% CO_2 was maintained at 37 °C. All the aforementioned experiments used 0.25% trypsin for cell dissociation, followed by a medium change and the plating of the resuspended cells.

2.12. Cellular uptake efficiency

A total of 5×10^5 HeLa cells was seeded in 35 mm confocal dishes and cultured overnight. Tumor cells were treated with 2.0 nM NC in 2 mL of DMEM complete growth medium at 0.5, 1.0, 1.5, and 2 h. The intracellular distribution of Au was analyzed using ICP-MS.

2.13. Cellular and nuclear quantification of GNR and NC

HeLa cells were grown at a density of 5×10^6 cells per 10 mL of culture medium on 10 cm Petri plates. The cells adhered for 24 h before being treated with GNR and NC for 12 h. After discarding the growth fluid and washing the plate three times with PBS, the cells were trypsinized and collected. The quantity of GNR and NC taken up by the nucleus was studied after the nuclei were removed from the HeLa cells. The nuclear material was removed using a solution containing 1 mM EDTA, 1% Triton X-100, 100 mM NaCl, and 10 mM Tris buffer (pH 7.4). At a temperature of 4 °C, the acquired cells had their nuclei removed. After incubation for 10 min, cell nuclei were extracted using centrifugation. Then, the cell nuclei were eliminated using a cell lysis solution containing 1 M NaOH and 0.5% Triton X-100. Nuclear absorption of GNR and NC was performed together with inductively coupled plasma atomic emission spectrometry (ICP-AES) to determine the concentration of gold. The cellular uptake of GNR and NC was detected using the aforementioned technique without the need to remove nuclei. Three independent experiments ($n = 3$) were performed for each data point.

2.14. *In vitro* biocompatibility and cytotoxicity

In a 96-well plate, 5000 HeLa cells were used to assess the cytotoxicity and biocompatibility of NC. After 24 h of co-culturing with NC at varying concentrations, the biocompatibility of the cells was evaluated. The cells in the photothermal group were exposed to an NIR laser at 808 nm for 5 min. Subsequently, the cell viability was assessed using the MTT assay following the protocol provided by the manufacturer.

2.15. Cell staining with calcein AM and propidium iodide dyes

Following the established protocol, we used calcein AM and propidium iodide (PI), respectively, to stain living and dead cells with and without NIR laser irradiation. A 24-well plate was seeded with 50 000 HeLa cells and left there overnight. The next day, the plate was placed in an NC incubator. After irradiation with an NIR laser, the cells in the sample well were grown for 12 h alongside the untreated, NIR only, and NC only cells. The HeLa were stained in a volume of 900 μL using a solution containing 2 μM calcein AM and 6 μM PI. Following a PBS wash of all the sample wells, fluorescence micrographs were obtained.

2.16. *In vitro* hemolysis assay

Fresh mouse blood stabilized with heparin and the red blood cells (RBCs) were obtained according to the previously reported protocol.[31] Then, 0.1 mL of a 10-fold diluted RBC solution was gently mixed with 0.9 mL of PBS containing NC at various concentrations (25, 50, 75, and 100 μg mL^{-1}, respectively). Each combination was left alone for 2 h at room temperature before being centrifuged at 10 000 rpm for 1 min. PBS and water were used as the positive and negative controls in two separate studies, respectively. The hemolysis percentage of different samples was calculated according to the following equation:

$$\text{Hemolysis percentage} (\%) = \frac{\text{Sample absorbance} - \text{Negative control absorbance}}{\text{Positive control absorbance} - \text{Negative control absorbance}} \times 100\%$$

2.17. Ethics statement and *in vivo* antitumor study

All *in vivo* animal studies were done in accordance with the guidelines authorized by the Institutional Review Board. Mice were used in the animal experiments after receiving prior clearance from the Institutional Animal Ethical Committee (IAEC), which was established by the Animal House Division. The experiments were conducted in accordance with the strict standards and recommendations from CPCSEA. The experiments and animal handling were performed according to the CPCSEA standards. The techniques followed the standards for the moral treatment of the animals. All Balb/c mice weighing 20 g were obtained from the Kerala Veterinary and Animal Sciences University, Animal Centre and maintained in suitable experimental conditions such as room temperature of 24 °C and 40–60% relative humidity, with a regular 12 h light–dark cycle. Animal usage was officially permitted by the IAEC, and *in vivo* animal experiments were carried out in agreement with the IAEC of the university. Prior to the *in vivo* trial, the test animals underwent a minimum of three days of acclimatization.

To construct the tumor model, the right posterior of the hind legs of the mice was injected with 1×10^6 U14 cells. When the tumor achieved a mean volume of ~100 mm^3, the

mice were randomized into four groups to examine the anti-cancer effects of NC (control, NC, NIR, and NC + NIR). In this context, PTT refers to a single 1 W cm^{-2} (808 nm) laser irradiation for 5 min. In the anticancer study, 100 µL of NC was injected intravenously into the mice in both the NC and NC with NIR groups. After injection, the mice were split into four groups, including control, free NC, NIR laser, and NIR with NC. Calipers was used to measure the tumors every three days during and after treatment. Relative tumor volumes were calculated by first adjusting the volume value to the original tumor size, and then dividing by the body mass of the mouse. Tumor volumes were calculated using the formula length (width) $2 \times 1/2$.

2.18. Tumor temperature measurement

An IR thermal camera (Testo 875-Germany) was employed to perform the tumor temperature analysis. Tumor-bearing mice were treated with control, NC, NIR, and NC with or without the wavelength of 808 nm at 1 W cm^{-2} for 5 min. During NIR irradiation with an 808 nm laser, the temperatures of the tumors were simultaneously recorded with an IR thermal camera.

2.19. Blood circulation analysis

We evaluated the pharmacokinetics of NC by detecting the concentration of Au in the mouse blood using ICP-MS. Briefly, 0.2 mL of NC suspension was injected intravenously into each tumor-bearing mouse. At 5, 12, 24, and 48 h after injecting mice, we collected blood for ICP-MS analysis.

2.20. Biodistributions of GNR

The tumor-bearing mice were randomized into two groups i.v. injected with NC and control mice (for gold: 5 mg kg^{-1}). At 6, 12, and 24 h post-administration, the mice were sacrificed for the systemic distribution analysis of NC. The major organs (heart, liver, spleen, lung, and kidney) in each group were collected and dissolved in digesting aqua regia solution. The concentrations of Au in the organs of each group were measured by ICP-AES. The collected tumors for each group were further divided into 2 parts (total tumor accumulation and nuclear uptake, $n = 4$ for each part). The total tumor accumulation was quantified after digesting by ICP-AES. To detect the nuclear uptake of NC, the tumor tissues were pretreated by Nuclear Extraction Kit according to the manufacturer's specification. The contents of Au in the nuclei were also determined by ICP-AES. The same processes were carried out for the analysis of the biodistribution of GNR.[45]

2.21. *In vivo* toxicity evaluation

Blood was collected and centrifuged from the tumor-bearing mice to test the levels of ALP (alkaline phosphatase), ALT (alanine aminotransferase), ALB (albumin), GGT (gamma-glutamyl transpeptidase), AST (aspartate aminotransferase), TBIL (total bilirubin), CK (creatine kinase), LDH (lactate dehydrogenase), BUN (blood urea nitrogen) and CREA (creatinine) in their serum.

2.22. Histological examinations

The tumor-bearing mice were divided in a total of four groups, *i.e.*, control, NC, NIR, and NC + NIR. The major organs (liver, lung, spleen, heart, and kidney) of the mice in the NC and NC with NIR groups were removed and stained with H&E after receiving 200 µL of NC (1 nM in PBS) intravenously. The bright field images were taken using an inverted microscope.

2.23. Detection of immunogenic cell death (ICD) markers

To evaluate the PTT-induced ICD in cancer cells, immuno-fluorescence was used to examine the surface CRT expression and the extracellular release of HMGB1 and HSP70. The seeding density of cancer cells in a 6-well plate was typically 2×10^5 cells per well. The cells were exposed to 808 nm at 1 W cm^{-2} for 5 min after a 6 h incubation period (control, NC group, NIR group, and NC with NIR group). Treatment with HMGB1, HSP70, and CRT-rabbit monoclonal antibodies was carried out for 1 h, and then the cells were washed twice with PBS before being stained with Alexa Fluor 488 or 594-goat anti-rabbit IgG. This process was repeated for a total of 24 h. After staining the cells with DAPI, they were observed using a laser scanning confocal microscope (LSCM) for 20 min. The ATP Assay Kit was used to assess the release of ATP. In summary, the cells were treated, and then cultured for 24 h. Following the instructions provided in the instruction manual, the conditioned medium was collected, and the ATP content was measured using a commercial ATP assay kit.

2.24. DC maturation

Tumor-specific immune cells were isolated and analyzed using flow cytometry, together with CD8$^+$ T cells, CD11c$^+$ CD86$^+$ CD80$^+$ DCs, CD4$^+$ FOXP3$^+$ T cells, and lymph nodes.

2.25. Cytokine detection

After the treatment of the mice, all the serum samples were obtained for further analysis. The levels of IL-2, TNF-α, and IFN-γ were measured with the help of enzyme-linked immunosorbent assay (ELISA) kits.

2.26. Statistical analysis

Experiments were performed in triplicate to derive mean ± standard deviation. The Student's *t*-test was used to assess the data. *$p < 0.05$ and **$p < 0.01$ represent the statistically significant date in the figure legends.

3. Results and discussion

In this study, the GNR-TAT peptide was conjugated using a simple mixing step according to the previous method.[44] After that, the targeting FA ligand-modified GNR nanoconjugate was prepared.[45] To improve its biocompatibility, PVP was introduced in the system. Then, ICG and R848 were loaded in GNR through the self-assembly method. R848 is a crucial immunological stimulant because it activates DCs TLRs, and ICG is an NIR dye with a strong photothermal effect. It is worth noting

that the two ingredients we chose are substances already in use in clinical settings and have been authorized by the Food and Drug Administration. The prepared GNR-TAT-FA@ICG-R848 nanocomposite was named NC. Polyvinylpyrrolidone (PVP) is a polymer approved by the FDA for use as a blood plasma expander, and thus its therapeutic effectiveness is well established. PVP has the potential to replace polyethylene glycol (PEG) in freeze-drying preparation processes due to its lyophilic and cryoprotectant properties. In addition, PVP has been shown to increase the solubility of micelles and interact with both hydrophilic and hydrophobic drugs.[49] We prepared the GNR based on the classic seed-mediated synthesis. The TEM image revealed a good dispersion of GNR (Fig. 1a). The UV-vis-NIR absorption spectra of the GNR seeds, GNR, ICG, and NC are shown in Fig. 1b. The absorption spectra for both the GNR and NC samples showed two peaks due to the extensive absorptions of GNR. The red shift in the maximum absorption peak from 780 to 820 nm

demonstrated that the encapsulation of ICG onto GNR led to an increase in particle size and a remarkable NIR-responsive characteristic of NC.[50] Fig. 1c shows the NIR absorption spectra of different concentrations of NC, including 25, 50, 75, and 100 μg mL^{-1}, indicating its broad and potent absorption band ranging from the visible to NIR region and covering the NIR window with obvious sharp peaks at 800 nm, which suggests that they can act as PTAs.

The chemical composition and crystallinity of GNR were studied by X-ray diffraction (Fig. 1d). The face-centered cubic structure of gold (JCPDS no. 04-0784) has characteristic diffraction peaks at 35.27°, 46.42°, and 63.70°, corresponding to the (111), (200), and (220) crystal planes, respectively.[51] These optical maxima indicate that GNR possessed a crystalline structure. In addition, the diffraction patterns reveal that our samples are made up of pure crystalline gold with no additional impurities. Fourier transform infrared spectroscopy (FTIR) is the most effective infrared spectroscopy method for
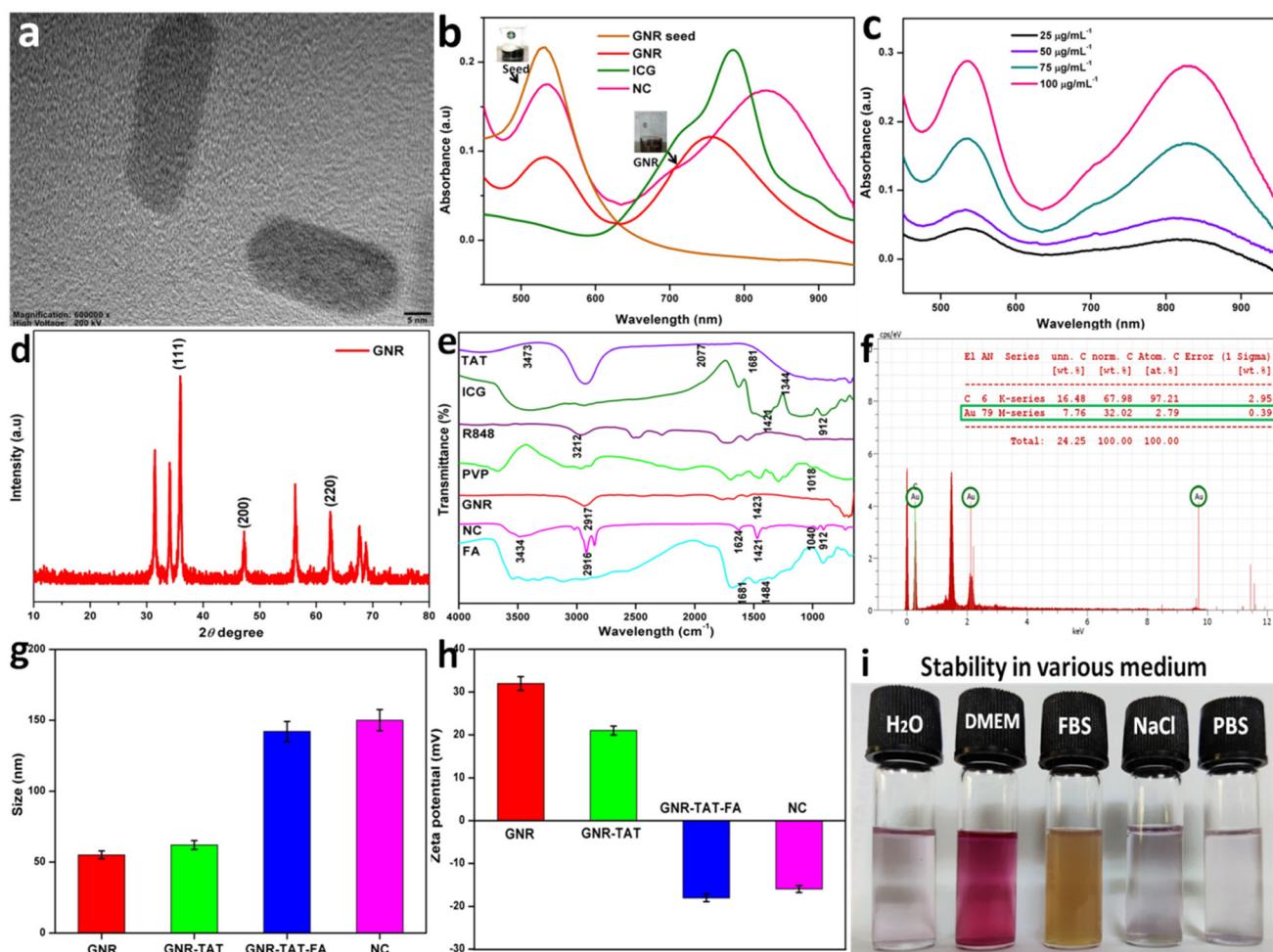
Fig. 1 (a) TEM image of GNR. (b) UV-vis-NIR spectra of synthesized GNR seed, GNR, ICG, and NC. (c) UV-vis-NIR spectra of synthesized NC at different concentrations include 25, 50, 75, and 100 μg mL^{-1}. (d) X-ray diffraction spectrum of GNR. (e) FTIR spectra of FA, TAT, ICG, R848, PVP, GNR, and NC. (f) Energy-dispersive X-ray analysis (EDX) of GNR (green circle shows the existence of gold). (g) DLS of GNR with indicated stepwise functionalization. (h) Zeta potential of GNR with indicated stepwise functionalization. (i) Photographs showing the stability of NC in various biological media.

characterizing the chemical structure of NC and locating the many molecules bound to NC. As shown in Fig. 1e, the FTIR spectrum of GNR exhibits two characteristic peaks at 2917 and 1423 cm^{-1}.[52] The presence of N–H group vibrations at 1484 and 1681 cm^{-1} and aromatic C–C stretching vibrations in the FTIR spectrum demonstrates that NC was successfully functionalized with FA. The typical O–H and C–H vibrational absorption peaks at 912 and 1421 cm^{-1} indicate that ICG was efficiently loaded in the NC. Coating R848 was effective, as shown by the stretching vibration peak of the hydroxyl groups in NC in the range of 3200 to 3500 cm^{-1}. TAT peptide molecules have a surface cap, as shown by the FTIR spectrum of NC, which exhibited intense bands at 3473, 2077, 1681, and 1344 cm^{-1}. In the FTIR spectrum of PVP, we observed weak CH$_2$ rock-

bending at 1018 cm^{-1}. After being loaded by NC, the amino acid C–O stretching peak shifted to a higher frequency at 1040 cm^{-1}. The characteristic peaks of NC at 3434, 2915, 1624, 1421, and 912 cm^{-1} confirmed the elements present in NC. The EDS results showed that the composite NPs were successfully prepared given that GNR possessed 32.02 wt% of Au and a high concentration of C atoms (Fig. 1f).[53] The size distribution of GNR, GNR-TAT, GNR-TAT-FA, and NC in solution was revealed by DLS measurement, which is about 55.3, 62.8, 142.3, and 150.2 nm, respectively. However, the NC DLS result is considered higher, which is due to the aggregation of NC (Fig. 1g). The zeta potential of GNR, GNR-TAT, GNR-TAT-FA, and NC was measured to be +32.4 mV, +21.6 mV, −18.1 mV, and −16.8 mV.[25] The negative charges of GNR-TAT-FA and NC
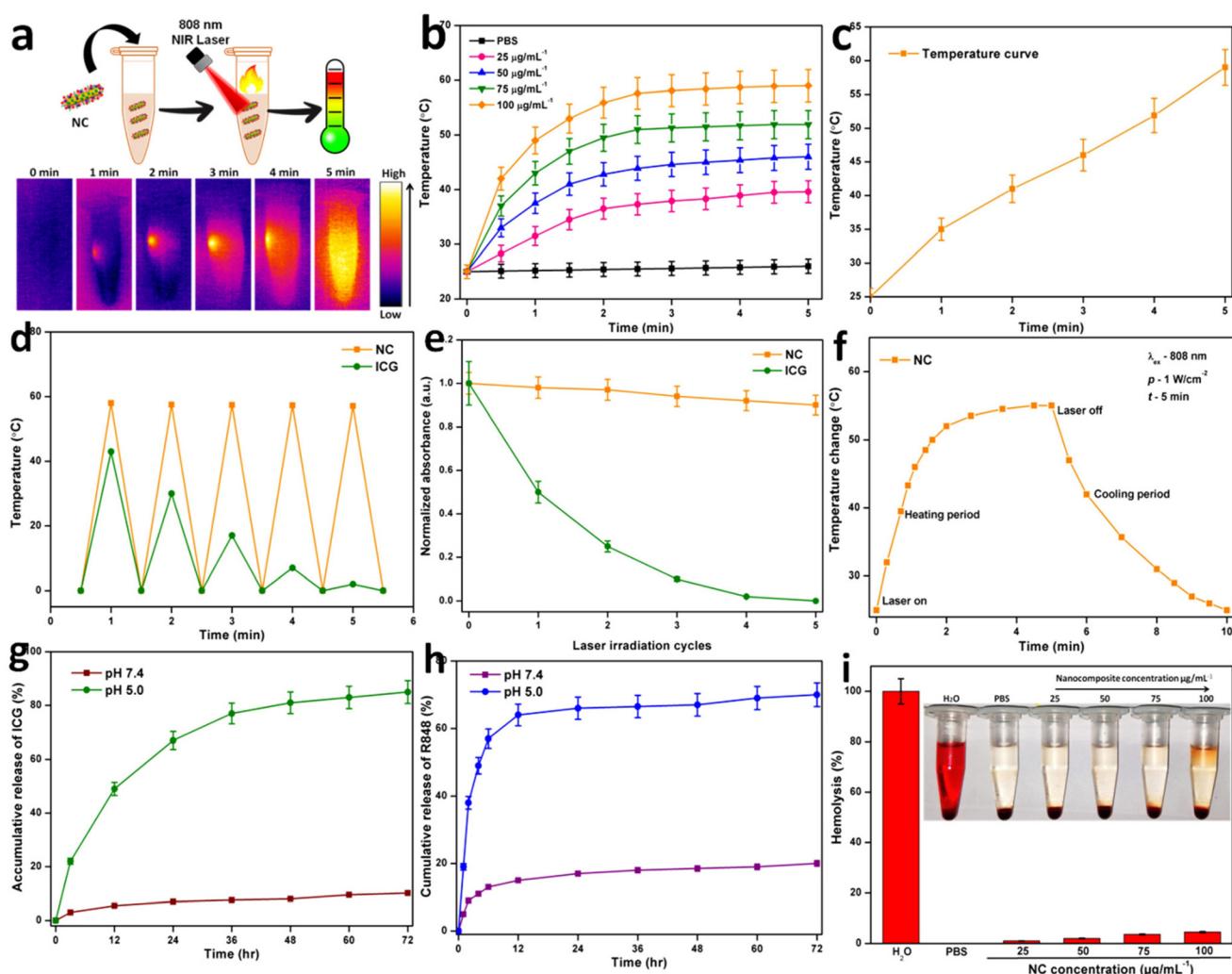

Fig. 2 (a) Thermal images of NC irradiated at 808 nm for 5 min. (b) Temperature change of PBS and NC at varying concentrations (25, 50, 75, and 100 µg mL^{-1}) under 808 nm laser irradiation (1.0 W cm^{-2}, 5 min). (c) Final temperature curve of NC. (d) Temperature change of free ICG and NC aqueous solution over five laser ON/OFF cycles under identical conditions. (e) Relative absorbance of NC and free ICG after being exposed to an 808 nm laser (1 W cm^{-2}) for 5 laser irradiation cycles (30 min each cycle 5 min). (f) Temperature curves of NC for 10 min under NIR (808 nm) laser irradiation. (g) Release profile of ICG from NC under various pH conditions. (h) Release profile of R848 from NC under different pH conditions. (i) Hemolysis percentage of RBCs incubated with NC at various concentrations of 25 µg mL^{-1}, 50 µg mL^{-1}, 75 µg mL^{-1}, and 100 µg mL^{-1} for 24 h, using DI water and PBS.

were due to the successful coating of FA. The uncoated GNR was discovered to have a positive zeta potential of 32.4 mV. As shown in Fig. 1h, when the positive TAT peptide was modified, the zeta potential of GNR-TAT decreased from 22.8 to 21.6 mV. The colloidal stability was also maintained for at least 7 days (Fig. 1i) by the modified NC in water, PBS, and cell-culture conditions.[54]

3.1. Photothermal properties of NC

Photothermal images were taken to determine the thermal properties and a temperature increase was noted. Fig. 2a shows that temperature gradually increased within 5 min. Different concentrations of NC were also tested for their photothermal properties. The concentration was shown to be directly related to the rate of temperature rise (ΔT). PBS and NC solutions of varying concentrations were irradiated with an 808 nm laser. After being exposed to radiation, the tempera-

ture of NC increased according to the power density of the irradiation source and the sample concentration. For example, ΔT of NC was 35.6 °C, 42.2 °C, 49.6 °C, and 59.5 °C for concentrations of 25, 50, 75, and 100 μg mL^{-1} after 5 min of 808 nm NIR laser irradiation at the power density of 1 W cm^{-2} (Fig. 2b). As shown in Fig. 2c, under 808 nm laser irradiation (1 W cm^{-2}), the final temperature of the different concentrations of NC increased to almost 60 °C within 5 min. As shown in Fig. 2d, the temperature elevation of NC showed no significant decrease in temperature after five cycles.[55] Its strong photostability in the NIR band was validated by five cycles of consistent conversion. However, due to the severe photobleaching and instability of pure ICG, its photothermal heating curve was significantly reduced throughout the heating and cooling cycles. Fig. 2e demonstrates that after five cycles of irradiation, the UV-vis-NIR absorbance of NC at 808 nm remained unchanged, whereas the absorbance of ICG
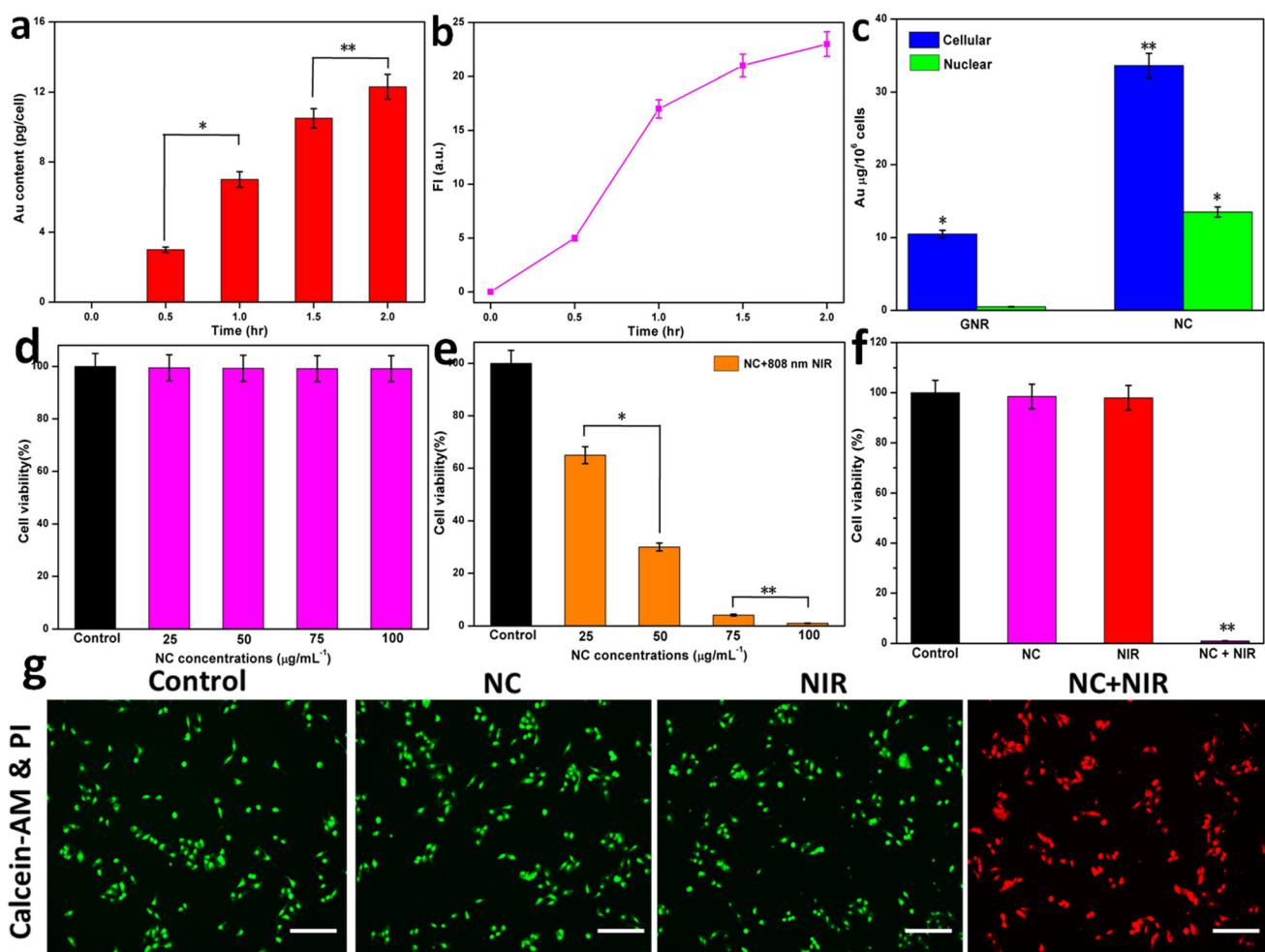
Fig. 3 (a) Gold content internalized in the tumor cells analyzed *via* ICP-MS. (b) Fluorescence intensity of NC. (c) Cellular and nuclear uptake amounts of GNR and NC by HeLa cells in 24 h of incubation. (d) HeLa cell viability assay after treatment with different concentrations of NC in the range 25–100 μg mL^{-1} for 24 h. (e) HeLa cell cytotoxicity assay after photothermal treatment with various concentrations of NC in the range 25–100 μg mL^{-1} for 24 h. (f) HeLa cell viability assay after treatment with control, NC, NIR, and NC with NIR for 24 h. (g) Live/dead staining images of HeLa cells treated with control, NC, NIR, NC with NIR. The scale bar in the panel represents 100 μm. Student's *t*-test, *$P < 0.05$; **$P < 0.01$ *versus* control.

at the same wavelength decreased significantly.[26] Subsequently, the photothermal properties of NC were analyzed to calculate its potential for hyperthermia. Photothermal conversion efficiency (PCE) measures how effectively NC converts laser energy into thermal energy. After 5 min of irradiation, the laser was turned off, and every 30 s, analysts checked NC to see how quickly it cooled down. The PCE (η) of NC was calculated to be 40.31% under 808 nm laser at a power density of 1 W cm^{-2} (Fig. 2f).[20] We compared the release of ICG from NC in a normal (pH = 7.4) and a tumorous (pH = 5.0) environment. In response to changes in pH, the π–π stacking interaction modulated the release of ICG from NC. NC released more ICG at longer intervals when the pH was low.

After 24 h in an acidic environment (pH = 5.0), over 60% of ICG was released, but under physiological conditions (pH = 7.4), ICG was released in much lower quantities.[56] The quick release of ICG at acidic pH may be due to the protonation of its tertiary nitrogen, which increases its water solubility and weakens the π–π stacking.

ICG could be encapsulated in FA-decorated NC to achieve targeted tumor theranostics, with its release occurring more slowly and in a smaller percentage than in the described system at the physiological pH. The drug release process is two-stage because the π–π stacking must be broken before the surface-coated TAT peptides can release the drug into the bloodstream (Fig. 2g). According to the comparison of the ICG
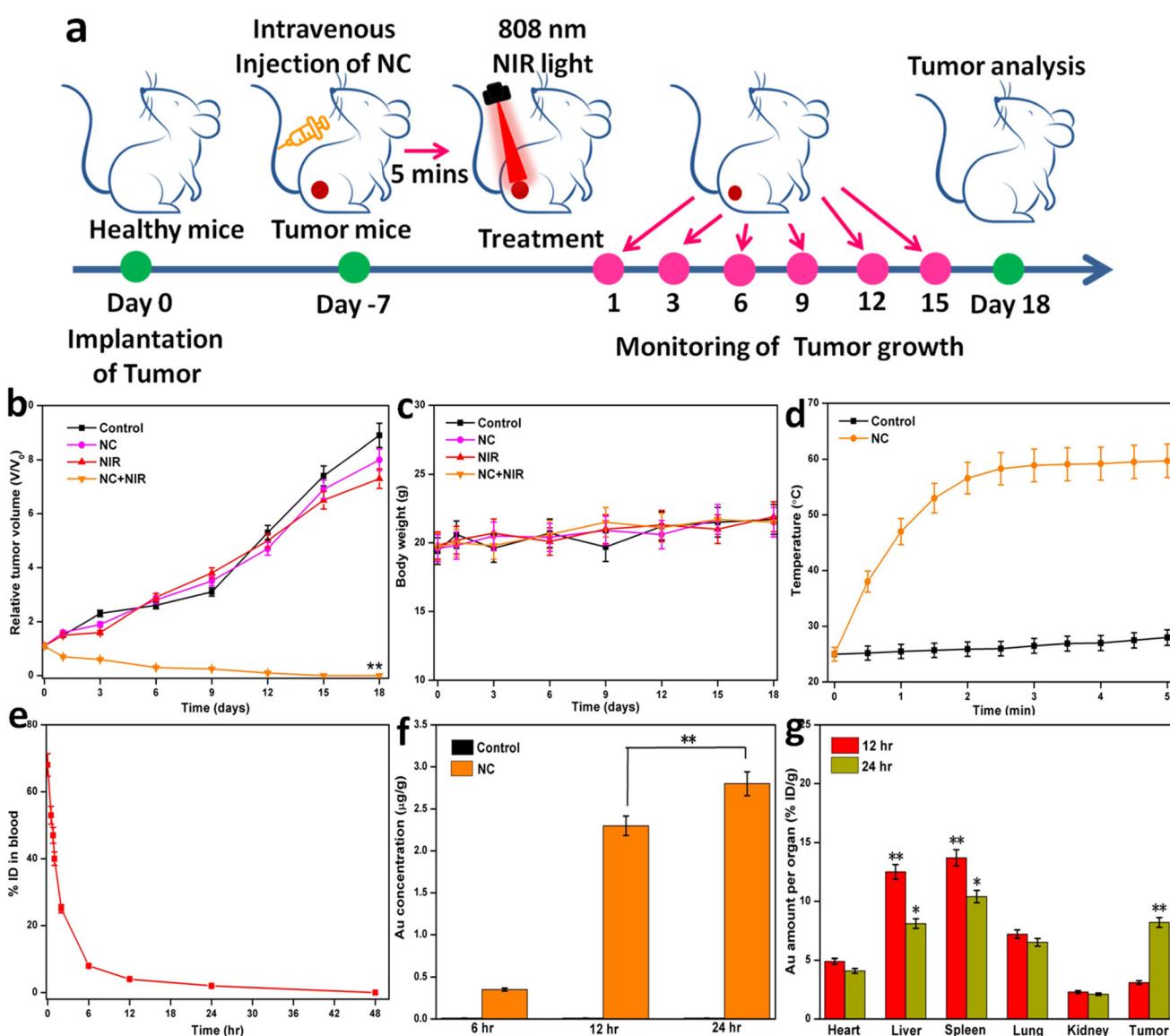

Fig. 4 (a) *In vivo* mice images to evaluate the recurrence of tumors after various treatments. (b) Tumor growth curves of mice after intravenous injection of different formulations. (c) Effects of NC on the body weight of mice bearing cells under 808 nm laser irradiation. Body weights were measured at the indicated time points. (d) Temperature changes of tumor-bearing mice injected with saline and NC at various time points. (e) NC circulation time after 48 h. (f) Quantification of Au in the nuclei of the tumor tissues 6, 12, and 24 h after intravenous injection of NC. (g) Biodistribution of NC in mice on the 1st day and 18th day of treatment. Student's *t*-test, *$P < 0.05$; **$P < 0.01$ *versus* control.

loading efficiency (LE) and loading capacity (LC), GNR was determined to have a greater value. The constant electrostatic interaction between the positively charged GNR and negatively charged SO_3^- groups on ICG accounts for the high loading capacity of GNR. Previously, researchers determined LC and LE values of 12.8% and 71.8%, respectively, for ICG release during loading.[2] After mixing R848 with GNR, the LC and EE of GNR were calculated. The LC and EE could be changed by changing how much R848 was added.[57] The EE was calculated to be 62.7% for R848 and its LC was 15.2%. The properties of R848 release were investigated under two different pH conditions. We found that the rate at which R848 was released from NC depended on the pH of the surrounding environment. At a pH of 5.0, the R848 release rate was 62.67%, but at the physiological pH of 7.4, it was just 19.75%. Most R848 is protonated in acidic environments, and it has notable water solubility under these conditions, which is likely the cause of the increased rate of R848 release (Fig. 2h). Hemocompatibility testing is required before NC can be used in other biological applications. In this study, RBCs were exposed to NC at concentrations in the range of 25 to 100 µg mL^{-1}. Fig. 2i shows the proportion of hemolysis. The findings demonstrated that the effect of NC on hemolysis was limited even at the highest dosage tested (100 µg mL^{-1}), indicating that the NC is hemocompatible.

3.2. *In vitro* cellular studies

To enhance the cellular absorption of chemotherapy drugs, they should be targeted directly to the tumor region without injuring the surrounding healthy tissue. Active targeting is a method of selectively killing cancer cells by connecting to them to a receptor or other surface feature of the cell.[58] An enhanced and more active targeting mechanism is necessary to increase the efficiency at which drug-containing nanocarriers are taken up by cancer cells at the tumor location. NPs contain many targeting moieties or ligands against receptors expressed on the surface of cancer cells immobilized on them to promote their absorption in cells through receptor-mediated endocytosis.[59] Folic acid (FA) is widely used as a targeting moiety in anti-cancer drugs. An interesting new type of actively targeted nanomaterials is drug conjugates with an incorporated nanovaccine (NV). Folate receptors (FR) are membrane proteins whose surface expression is regulated by individual cells. Due to their high folate requirements, cancer cells often
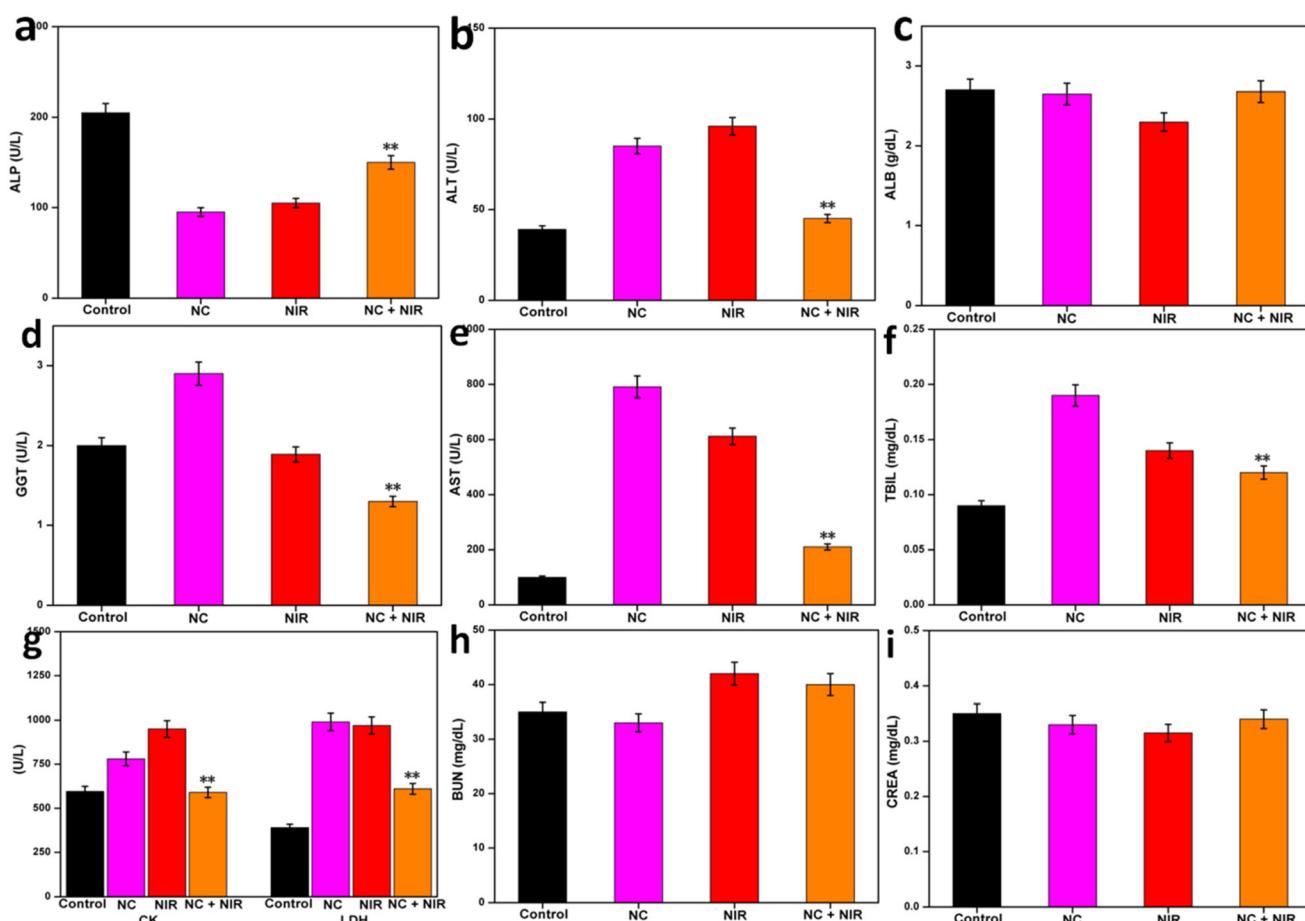
Fig. 5 Serum biochemical examination of NC-treated mice. Female BALB/c mice served as the control group. Data presented as mean (SD) (n = 5). (a) ALP, alkaline phosphatase. (b) ALT, alanine aminotransferase. (c) ALB, albumin. (d) GGT, gamma-glutamyl transpeptidase. (e) AST, aspartate transaminase. (f) TBIL, total bilirubin. (g) CK, creatine kinase, LDH, lactate dehydrogenase. (h) BUN, blood urea nitrogen. (i) CREA, creatinine.

overexpress FR.[2] Given that folate is essential for DNA nucleotide synthesis and cell division, cancer cells need much more of it than normal cells. In this case, FR is a suggested targeted site given that it is under expressed in normal tissues but highly expressed in tumors. One of the advantages of FA is that it may be coupled with other nanotechnology platforms, such as GNPs and chemotherapeutic drugs.[60] After 2 h of incubation, as shown in Fig. 3a, HeLa cells quickly internalized NC. Inductively coupled plasma mass spectrometry (ICP-MS) was used to measure the amount of Au in the HeLa cells, and hence the amount of NC taken up. Incubation for 2 h resulted in a maximum gold concentration of 12.3 pg per cell. Fig. 3b displays the results of the *in vitro* analysis of NC uptake and subsequent fluorescence activation by the cells. The HeLa cells were treated with NC loaded with ICG. The intriguing observation was the enhanced fluorescence in the NC-treated cells. After 2 h, NC exhibited a higher intracellular absorption rate, as shown by the activation of ICG fluorescence inside the cells.

The ICP-AES analysis of the cellular and nuclear GNR and NC uptake is shown in Fig. 3c. Conjugation with FA and TAT greatly enhanced the cellular uptake of NC and resulted in the intranuclear localization of GNR. These results corroborate previous research showing that the TAT peptide aids in the nuclear translocation of GNR.[44] The biocompatibility of NC

was tested *in vitro* by a viability experiment using HeLa cells. The remarkable biocompatibility of the multifunctional NC was shown by the fact that the viability of HeLa cells was maintained at more than 98% after treatment with concentrations in the range of 25 to 100 μg mL^{-1} (Fig. 3d). Different concentrations of NC were used to determine the viability of the cells. At concentrations of 25, 50, 75, and 100 μg mL^{-1}, the photothermal effects on the cells were identified, leading to a significant decrease in cell viability (% viability). An 808 nm NIR laser (1 W cm^{-2} for 5 min) was used to induce PTT in NC. A 1 W cm^{-2} NIR laser increased the temperature of ICG-loaded NC, whereas a higher NC concentration (100 μg mL^{-1}) enhanced PTT. The photothermal property of NC was responsible for the significant increase in temperature. At NC concentrations of 25 and 50 μg mL^{-1}, the cell viability drastically decreased by around 65% and 30%, respectively. Furthermore, the cell viability was significantly reduced by photothermal stress at NC concentrations of 75 and 100 μg mL^{-1}, by around 5% and almost 100%, respectively. This reveals that ICG-loaded NC was efficiently ablated by photothermal energy when exposed to NIR (Fig. 3e). Furthermore, NC, NIR, and NC with NIR showed a difference in cell viabilities such as NC and NIR did not cause a significant reduction in the levels of cell viability. However, NC with NIR depicted a significantly high
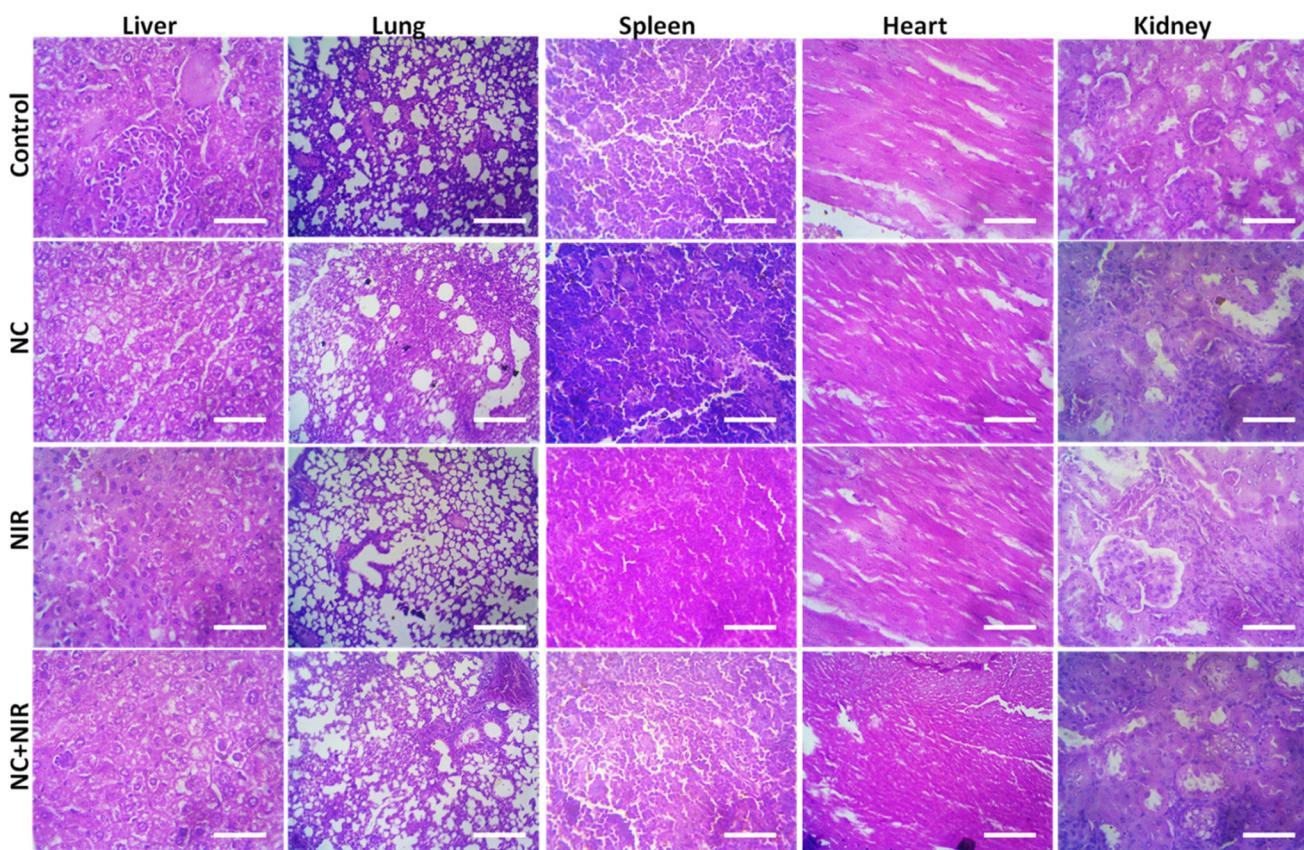

Fig. 6 Histological images of H&E-stained tissue sections of the liver, lung, spleen, heart, and kidney from the mice that received a targeted PTT at the power density of 1 W cm^{-2} followed by post-injection. Scale bar: 100 μm.

reduction in the level of cell viability due to the efficient targeted photothermal ablation of ICG-loaded NC (Fig. 3f). Calcein-AM (green, alive) and propidium iodide (PI) (red, dead) reagents were used in a dual-staining approach to assess the cell viability. Also, the control, NC, NIR, or NC with NIR groups were exposed to 808 nm laser irradiation (1 W cm^{-2}) for 5 min. No cytotoxicity was seen in the control, NC, or NIR groups, indicating that these NCs could potentially be used as safe agents (Fig. 3g).

3.3. *In vivo* studies for NC

Five tumor-bearing mice were randomly assigned to one of four groups (control, NC, NIR, and NC + NIR) for *in vivo* anti-cancer therapy. The samples were injected intravenously into the tail veins of the tumor-bearing mice on day one and three of the experiment. After injecting the tumor, a laser with a wavelength of 808 nm (1 W cm^{-2} for 5 min) was focused on it (NIR and NC with NIR group). Except for NC with the NIR group, the relative tumor volumes were significantly larger after 18 days compared with the initial volumes. Compared to the other three groups, the tumor growth was drastically reduced in the NC with the NIR laser group. Fig. 4a and b demonstrated that the targeted PTT effectively inhibited tumor growth. Furthermore, no obvious weight loss was observed across all groups during the duration of therapy, showing that our NC system did not influence the body weight of the animals (Fig. 4c).

To monitor the PTT effects of NC *in vivo*, an IR thermal imaging camera was also employed to detect the increase in temperature at the tumor site when it was irradiated with an 808 nm laser. The tumors injected with NC attained temperatures of over 55 °C after being exposed to a 1 W cm^{-2} laser for 5 min. However, when exposed to the same levels of radiation, the control mice exhibited no signs of heat stress. These findings verified the efficacy of ICG-loaded GNR as light-absorbing agents, leading to the generation of heat, and the remarkable selectivity of the PTT activities of NC (Fig. 4d). Successful cancer treatment relies on therapeutic NC with lengthy circulatory lifetimes accumulating in tumors after systemic injection. Thus, the Au concentrations in the blood were measured to evaluate the pharmacokinetics of NC, providing insight into whether this compound is suitable for usage *in vivo*. The half-life of NC was calculated to be 52 min. By reducing its nonspecific adhesion to blood components and providing adequate stealth, it was anticipated that the long half-life of NC would delay its metabolic clearance and
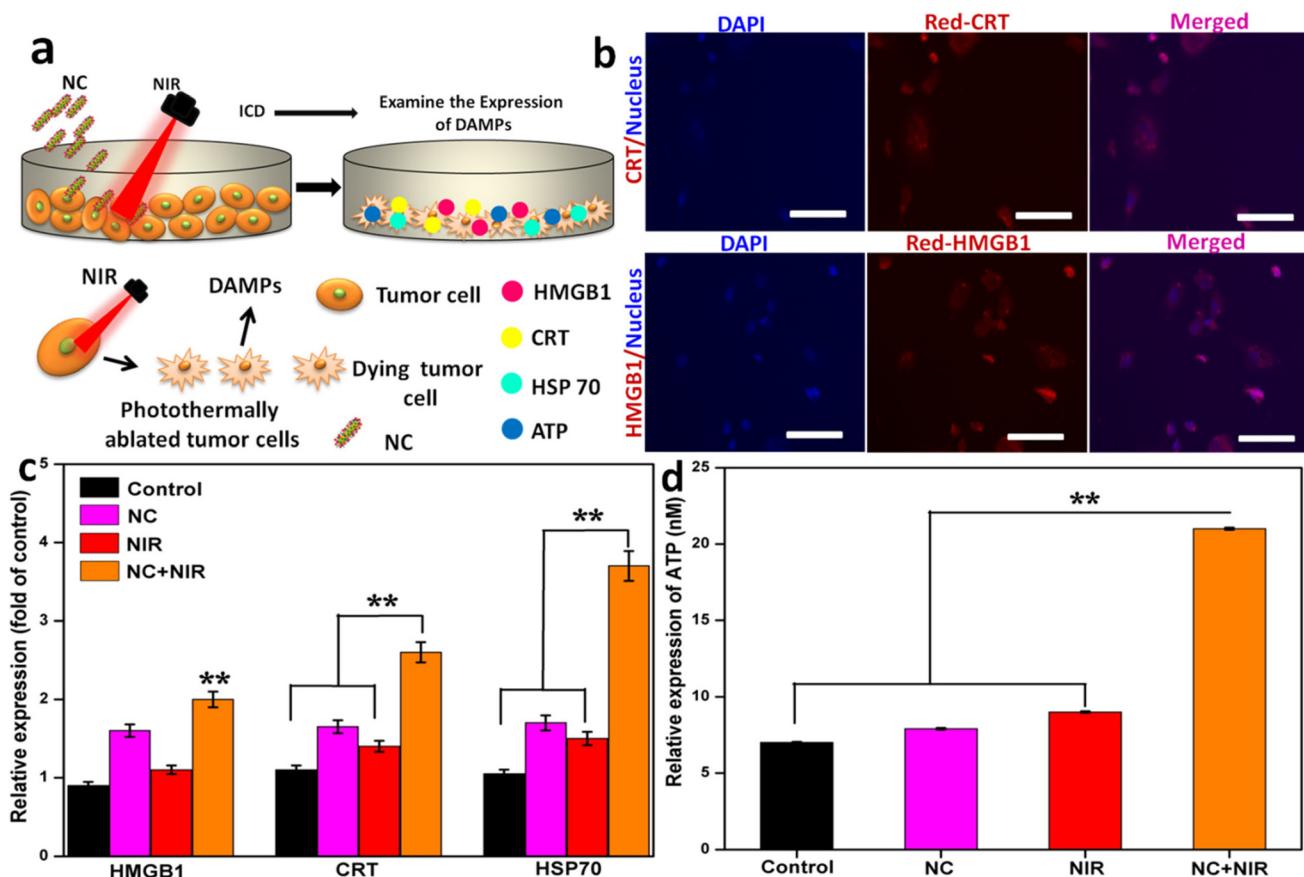

Fig. 7 (a) Schematic illustration of the experiment. (b) Immunofluorescence analysis of HMGB1, and CRT expression after the above-indicated treatment. Scale bar: 20 μm. (c) Quantitative analysis of HMGB1, CRT, and HSP70. (d) ATP expression. (Mean ± S.D., *n* = 3. Student's *t*-test, *P < 0.05; **P < 0.01 *vs.* control).

extend its time in the circulation (Fig. 4e). Also, at 24 h post-injection, the nuclear uptake of NC was as high as 2.9 µg g^{-1} Au, whereas the control uptake was negligible. Consistent with *in vitro* investigations, greater tumor accumulation and dramatically enhanced nuclear absorption of NC are useful for boosting the nuclear PTT efficacy (Fig. 4f). After we discovered that NC efficiently interacts with the nucleus of cancer cells, we decided to look into its therapeutic potential using a mouse tumor model. The biodistributions of GNR in the tumor and major organs (heart, liver, spleen, lung, and kidney) were first assessed 12 and 24 h after intravenous injections of NC (Fig. 4g). The reticuloendothelial systems of the liver and spleen absorbed the majority of the injected NC. After 12 h, the gold content in the tumor was 3.17 ID g^{-1}, but by 24 h, it increased to 8.24 ID g^{-1}.

To further prove the efficacy of the treatment, serum biochemical markers were evaluated. Because NC is safe, there were no noticeable differences in biochemical markers in the liver, heart, and kidney between the tumor-bearing mice and the normal mice (control). After laser treatment for NC, biochemical markers of organ function returned to normal, indicating that tumor progression was prevented. No further biochemical abnormality in the blood was found when other NC formulations were employed (Fig. 5a–i).[61]

The tumor-bearing mice in all three treatment groups were sacrificed, and their livers, lungs, spleens, hearts, and kidneys were examined for evidence of damage. There were no discernible morphological differences among these groups, as seen in Fig. 6. Hematoxylin and eosin (H&E) staining of liver, lung, spleen, heart, and kidney tissues revealed no evident damage.
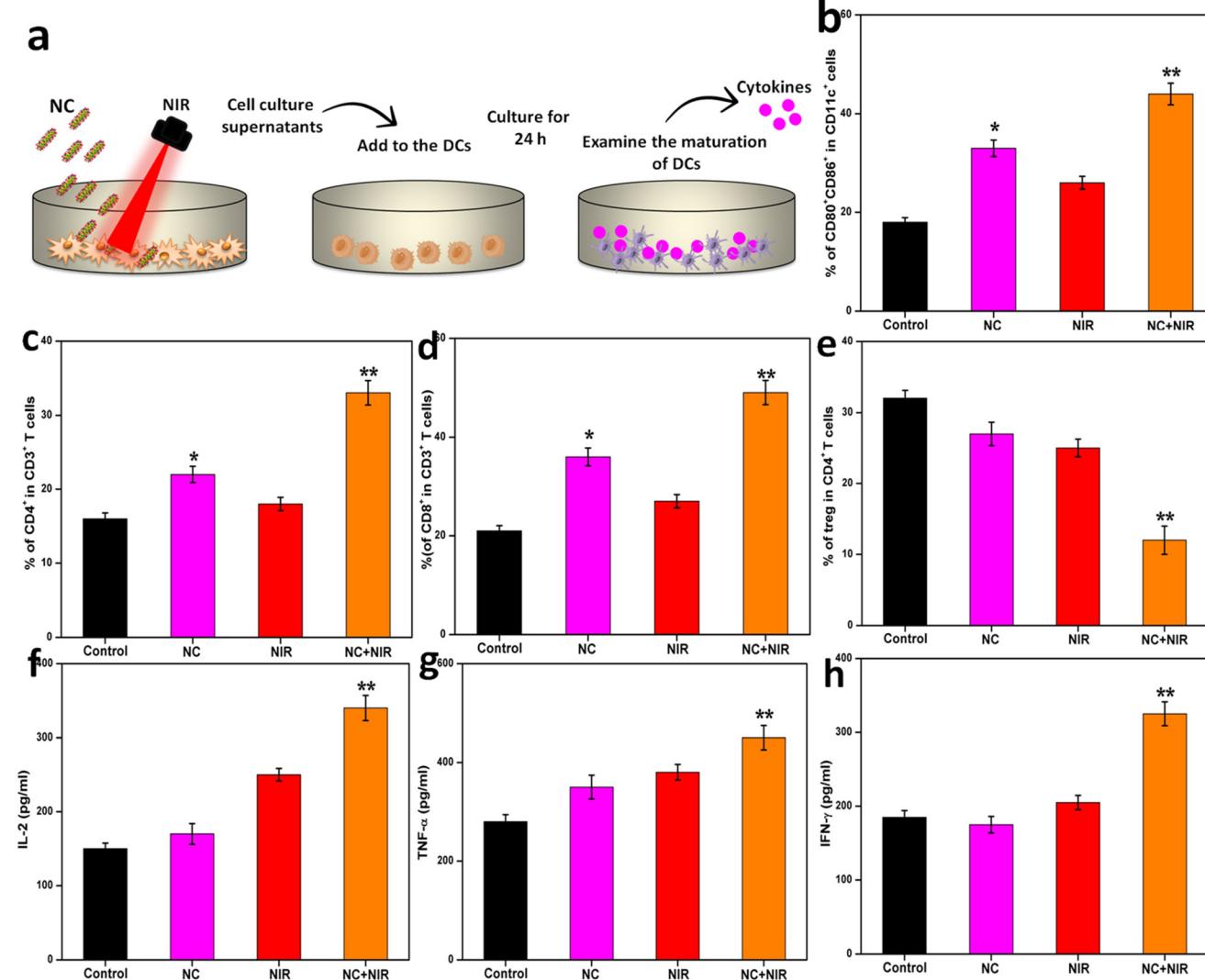
Fig. 8 (a) Schematic illustration of the experiment. (b) Immunosuppressive tumor environment quantitative analysis of matured DCs in lymph node (CD80$^+$CD86$^+$ gated on CD11c$^+$ cells) on day 18 after different treatments. (c) and (d) Quantitative analysis of CD4$^+$ and CD8$^+$ T cells (gated on CD3$^+$ T cells) in the tumor on day 18 after different treatments. (e) Percentage (gated on CD4$^+$ T cells) of Tregs in primary tumors on day 18 after the indicated treatments. (f), (g), and (h) Contents of IL-2, TNF-α, and IFN-γ in tumor tissues after the indicated treatment on day 18. Mean ± S.D., *n* = 4. Student's *t*-test, *P < 0.05; **P < 0.01 *versus* control.

3.4. Photothermal therapy-mediated immunogenic cell death and immunotherapy

We investigated whether the NC system may cause ICD post-PTT. The ICD in cancer cells is characterized by the production of known DAMPs such as CRT, HMGB1, ATP, and heat shock protein 70 (HSP70) (Fig. 7a). To generate a current, the cancer cells were exposed to laser light at 808 nm (1 W cm^{-2}) from a signal generator after being pre-incubated with NC. After NC treatment, the irradiation duration required to induce ICD as the aforementioned DAMPs in cancer cells was initially discovered. In response to irradiation, NC caused membrane CRT exposure, leading to the release of HMGB1 from the nucleus. Compared to the NC with NIR group, the NC with laser irradiation group had similar amounts of CRT exposure and HMGB1 release, indicating that ICD was caused by the photothermal effects of NC. Similar trends in DAMP synthesis were also seen by immunofluorescence (Fig. 7b), validating these results. The release of HMGB1, CRT, HSP 70, and ATP was significantly lower in the non-irradiated (NC and control) group compared to the irradiated group (Fig. 7c and d, respectively). These findings suggest that ICD was successfully induced by the photothermal conversion of NC utilizing NIR irradiation.

The blood levels of important immune cell cytokines were assessed, and the response of immune cells in lymph nodes, tumors, and spleens was measured to better understand how NC exerts its enhanced anticancer effect. DCs are essential for the maturation of both innate and adaptive immune responses, as seen in Fig. 8a. We tested the efficacy of a photoactivable NC-integrated R848 method to stimulate DC maturation in the inguinal lymph nodes. Fig. 8b shows that the NC group had a considerably higher percentage of mature DCs (CD80$^+$CD86$^+$CD11c$^+$) than the control group. The tumors were also analyzed to determine the presence of CD4$^+$ cytotoxic T lymphocytes (CTLs) and CD3$^+$ helper T cells. The tumors treated with NIR had a higher number of CD8$^+$ T cells and CD3$^+$ T cells compared to the controls, indicating that the antitumor immune response was successfully triggered. The disruption of R848 by photoactivatable NC seems to play a crucial role in avoiding the widespread depletion of T cells *via* DC maturation in tumors, as shown by the substantial increase in intratumoral infiltration of CD8$^+$ CTLs after treatment with NIR. In the NC or NIR group, the percentage of CD8$^+$ T cells and CD4$^+$ T cells was significantly higher than that in the control group. As demonstrated in Fig. 8c and d, there was no difference in the CD8$^+$ T cell population among the NC, NIR, and control groups, demonstrating that the naive T cells rapidly differentiated into CD8$^+$ T cells.

As shown in Fig. 8e, the Treg frequency in the NC with NIR group significantly decreased than that in the control group. Moreover, the NC with NIR group showed significantly increased levels of IL-12, IFN-γ, and TNF-α, which are the key biomarkers released by immune cells in the TME for altering T-cell responses (Fig. 8f–h). Taken together, these results demonstrate the possibility that the NIR-triggered photothermal NC method may sensitize cancers with an active immune response.

4. Conclusion

Ultimately, an ICG-loaded GNR NC was developed for the treatment of cervical cancer targeted therapy. The prepared NC was biocompatible and maintained a constant temperature under UV-visible NIR light. Direct tumor killing by NIR-induced PTT was possible, and potent *in vitro* and *in vivo* immune responses could be produced by loading an immunoadjuvant. NIR laser therapy with NC was shown to inhibit tumor growth, and also improve the long-term antitumor immunity, both of which may hinder cancer recurrence. In clinical settings, we believe that combining PTT with immunotherapy using GNR with an immunoadjuvant has significant potential for the treatment of cancer. Because of its ability to precisely control drug release and its built-in capability to monitor prodrug activation and active drug release, NC-based technology opens up a new door for the development of theranostic nanomedicine. This strategy may be able to kill cancer cells and stop them from returning in a single stroke. Furthermore, the results presented herein suggest that this method may help improve the effectiveness of cancer therapies.

Conflicts of interest

The author declares no competing financial interest.

Acknowledgements

References

1 R. L. Siegel, K. D. Miller, H. E. Fuchs and A. Jemal, *CA-Cancer J. Clin.*, 2022, **72**, 7–33.
2 K. Gowsalya, L. Karthikeyan and R. Vivek, *ACS Appl. Nano Mater.*, 2022, **5**, 17105–17122.
3 K. Gowsalya, B. Rithisa, Y. Haldorai, K. Shanthi and R. Vivek, *Nanomedicine*, 2024, **57**, 102738.
4 W. Y. Sheng and L. Huang, *Pharm. Res.*, 2011, **28**, 200–214.
5 U. Anand, A. Dey, A. K. S. Chandel, R. Sanyal, A. Mishra, D. K. Pandey, V. De Falco, A. Upadhyay, R. Kandimalla, A. Chaudhary, J. K. Dhanjal, S. Dewanjee, J. Vallamkondu and J. M. Pérez de la Lastra, *Genes Dis.*, 2022, 1367–1401.
6 Y. Yao, Y. Zhou, L. Liu, Y. Xu, Q. Chen, Y. Wang, S. Wu, Y. Deng, J. Zhang and A. Shao, *Front. Mol. Biosci.*, 2020, **7**, 193.
7 R. Vivek, V. NipunBabu, C. Rejeeth, A. Sharma, T. Ponraj, A. Vasanthakumar and S. Kannan, *Photodiagn. Photodyn. Ther.*, 2018, **23**, 244–253.
8 A. G. Niculescu and A. M. Grumezescu, *Polymers*, 2022, **23**, 421.

9 M. L. Taylor, R. E. Wilson Jr., K. D. Amrhein and X. Huang, *Bioengineering*, 2022, **9**, 200.

10 R. Vivek, R. Thangam, V. NipunBabu, C. Rejeeth, S. Sivasubramanian, P. Gunasekaran, K. Muthuchelian and S. Kannan, *ACS Appl. Mater. Interfaces*, 2014, **6**, 6469.

11 L. Zheng, X. Hu, H. Wu, L. Mo, S. Xie, J. Li, C. Peng, S. Xu, L. Qiu and W. Tan, *J. Am. Chem. Soc.*, 2020, **142**, 382–391.

12 W. Xu, J. Qian, G. Hou, Y. Wang, J. Wang, T. Sun, L. Ji, A. Suo and Y. Yao, *Acta Biomater.*, 2018, **82**, 171–183.

13 K. Xia, L. Zhang, Y. Huang and Z. Lu, *J. Nanosci. Nanotechnol.*, 2015, **15**, 63–73.

14 X. Duan, C. Chan and W. Lin, *Angew. Chem., Int. Ed.*, 2019, **58**, 670–680.

15 L. Wang, R. Vivek, W. Wu, G. Wang and J.-Y. Wang, *ACS Biomater. Sci. Eng.*, 2018, **4**, 1880–1890.

16 H. Kim, K. Chung, S. Lee, D. H. Kim and H. Lee, *Wiley Interdiscip. Rev.: Nanomed. Nanobiotechnol.*, 2016, **8**, 23–45.

17 V. Yasothamani and R. Vivek, *J. Mater. Chem. B*, 2022, **10**, 6392.

18 Y. Zhang, T. Wang, Y. Tian, C. Zhang, K. Ge, J. Zhang, J. Chang and H. Wang, *Acta Pharm. Sin. B*, 2021, **11**, 1978–1992.

19 L. Xie, X. Ying, X. Li, X. Tan, T. Zhang, X. Zhang, W. Cai, F. An, X. Liu and S. Han, *Mater. Des.*, 2023, **225**, 111456.

20 W. Yim, R. M. Borum, J. Zhou, Y. Mantri, Z. Wu, J. Zhou, Z. Jin, M. Creyer and J. V. Jokerst, *Nanotheranostics*, 2022, **6**, 79–90.

21 B. Zhou, J. Song, M. Wang, X. Wang, J. Wang, E. W. Howard, F. Zhou, J. Qu and W. R. Chen, *Nanoscale*, 2018, **10**, 21640–21647.

22 Z. Du, K. Yan, Y. Cao, Y. Li, Y. Yao and G. Yang, *Mater. Sci. Eng., C*, 2020, **117**, 111340.

23 C. You, Y. Li, Y. Dong, L. Ning, Y. Zhang, L. Yao and F. Wang, *ACS Biomater. Sci. Eng.*, 2020, **6**, 1535–1542.

24 L. M. Pan, J. N. Liu, Q. J. He and J. L. Shi, *Adv. Mater.*, 2014, **26**, 6742–6748.

25 L. M. Pan, J. A. Liu and J. L. Shi, *ACS Appl. Mater. Interfaces*, 2017, **9**, 15952–15961.

26 Y. Hu, R. Wang, Y. Zhou, N. Yu, Z. Chen, D. Gao, X. Shi and M. Shen, *J. Mater. Chem. B*, 2018, **6**, 6122–6132.

27 H. Wang, X. Li, B. W. Tse, H. Yang, C. A. Thorling, Y. Liu, M. Touraud, J. B. Chouane, X. Liu, M. S. Roberts and X. Liang, *Theranostics*, 2018, **8**, 1227–1242.

28 K. Gowsalya, V. Yasothamani and R. Vivek, *Nanoscale Adv.*, 2021, **3**, 3332.

29 H. Tang, X. Xu, Y. Chen, H. Xin, T. Wan, B. Li, H. Pan, D. Li and Y. Ping, *Adv. Mater.*, 2021, **33**, 2006003.

30 L. Karthikeyan and R. Vivek, *Adv. Cancer Biol.: Metastasis*, 2022, **4**, 100044.

31 S. Sobhana, N. P. Sarathy, L. Karthikeyan, K. Shanthi and R. Vivek, *Nanotheranostics*, 2023, **7**, 41–60.

32 L. Tang, A. Zhang, Z. Zhang, Q. Zhao, J. Li, Y. Mei, Y. Yin and W. Wang, *Cancer Commun.*, 2022, **42**, 141–163.

33 S. Musetti and L. Huang, *ACS Nano*, 2018, **12**, 11740–11755.

34 X. Fang, H. Lan and K. Jin, *Cancers*, 2022, **14**, 3842.

35 L. Karthikeyan, V. Yasothamani, Y. Haldorai, J. R. S. Selvan Christyraj and R. Vivek, *ACS Appl. Nano Mater.*, 2023, **6**, 6279–6291.

36 V. Yasothamani, L. Karthikeyan, S. Shyamsivappan, Y. Haldorai, D. Seetha and R. Vivek, *Biomacromolecules*, 2021, **22**, 2472–2490.

37 V. Yasothamani, L. Karthikeyan, N. P. Sarathy and R. Vivek, *ACS Appl. Bio Mater.*, 2021, **4**, 6575.

38 L. Karthikeyan, S. Sobhana, V. Yasothamani, K. Gowsalya and R. Vivek, *Biomed. Eng. Adv.*, 2023, **5**, 100082.

39 J. C. Li, X. R. Yu, Y. Y. Jiang, S. S. He, Y. Zhang, Y. Luo and K. Y. Pu, *Adv. Mater.*, 2021, **33**, 2003458.

40 Y. P. Jia, K. Shi, F. Yang, J. F. Liao, R. X. Han, L. P. Yuan, Y. Hao, M. Pan, Y. Xiao, Z. Y. Qian and X. W. Wei, *Adv. Funct. Mater.*, 2020, **30**, 2001059.

41 K. A. Michaelis, M. A. Norgard, X. Zhu, P. R. Levasseur, S. Sivagnanam, S. M. Liudahl, K. G. Burfeind, B. Olson, K. R. Pelz, D. M. Angeles Ramos, H. C. Maurer, K. P. Olive, L. M. Coussens, T. K. Morgan and D. L. Marks, *Nat. Commun.*, 2019, **10**, 4682.

42 J. Wagner, D. Gossl, N. Ustyanovska, M. Y. Xiong, D. Hauser, O. Zhuzhgova, S. Hocevar, B. Taskoparan, L. Poller, S. Datz, H. Engelke, Y. Daali, T. Bein and C. Bourquin, *ACS Nano*, 2021, **15**, 4450–4466.

43 L. R. Guo, D. D. Yan, D. F. Yang, Y. J. Li, X. D. Wang, O. Zalewski, B. F. Yan and W. Lu, *ACS Nano*, 2014, **8**, 5670–5681.

44 W. Tang, L. Han, X. Lu, Z. Wang, F. Liu, Y. Li, S. Liu, S. Liu, R. Tian, J. Liu and B. Ding, *ACS Appl. Mater. Interfaces*, 2021, **13**, 20974–20981.

45 P. Manivasagan, S. W. Jun, V. T. Nguyen, N. T. P. Truong, G. Hoang, S. Mondal, M. Santha Moorthy, H. Kim, T. T. Vy Phan, V. H. M. Doan, C.-S. Kim and J. Oh, *J. Mater. Chem. B*, 2019, **7**, 3811–3825.

46 K. Gowsalya, L. Karthikeyan and R. Vivek, *ACS Appl. Nano Mater.*, 2022, **5**, 17105.

47 Z. Sun, T. J. Fan, Q. Liu, L. D. Huang, W. B. Hu, L. L. Shi, Z. Z. Wu, Q. H. Yang, L. P. Liu and H. Zhang, *Nanophotonics*, 2021, **10**, 2519–2535.

48 Z. Y. Shi, C. C. Chu, Y. Zhang, Z. J. Su, H. R. Lin, X. Pang, X. Y. Wang, G. Liu and W. G. Li, *J. Biomed. Nanotechnol.*, 2018, **14**, 1934–1943.

49 C. Z. Jia, H. W. Liu, Y. X. Hu, H. Wu, C. P. Zhu, Y. X. Zhang, S. G. Wang and M. X. Huang, *ChemistrySelect*, 2021, **6**, 6564.

50 C. Leng, X. Zhang, F. Xu, Y. Yuan, H. Pei, Z. Sun, L. Li and Z. Bao, *Small*, 2018, **14**, 1703077.

51 N. T. Ha Lien, A. D. Phan, B. T. Van Khanh, N. T. Thuy, N. Trong Nghia, H. T. My Nhung, T. Hong Nhung, D. Quang Hoa, V. Duong and N. Minh Hue, *ACS Omega*, 2020, **5**, 20231–20237.

52 H. R. de Barros, L. Piovan, G. L. Sassaki, D. de Araujo Sabry, N. Mattoso, Á. M. Nunes, M. R. Meneghetti and I. C. Riegel-Vidotti, *Carbohydr. Polym.*, 2016, **152**, 479–486.

53 T. Ramasamy, H. B. Ruttala, P. Sundaramoorthy, B. K. Poudel, Y. S. Youn, S. K. Ku, H.-G. Choi, C. S. Yong and J. O. Kim, *NPG Asia Mater.*, 2018, **10**, 197–216.

54 S. Wang, X. Zhao, S. Wang, J. Qian and S. He, *ACS Appl. Mater. Interfaces*, 2016, **8**, 24368–24384.

55 S. K. Maji, S. Yu, E. Choi, J. W. Lim, D. Jang, G.-y. Kim, S. Kim, H. Lee and D. H. Kim, *ACS Omega*, 2022, **7**, 15186–15199.

56 J. Wu, G. R. Williams, S. Niu, F. Gao, R. Tang and L.-M. Zhu, *Adv. Sci.*, 2019, **6**, 1802001.

57 Y. Y. Liu, L. N. Qiao, S. P. Zhang, G. Y. Wan, B. W. Chen, P. Zhou, N. Zhang and Y. S. Wang, *Acta Biomater.*, 2018, **66**, 310–324.

58 W. J. Jiang, F. Mo, X. Jin, L. Chen, L. J. Xu, L. Q. Guo and F. F. Fu, *Adv. Mater. Interfaces*, 2017, **4**, 1700425.

59 L. Chen, L. L. Zhou, C. H. Wang, Y. Han, Y. L. Lu, J. Liu, X. C. Hu, T. M. Yao, Y. Lin, S. J. Liang, S. Shi and C. Y. Dong, *Adv. Mater.*, 2019, **31**, 1904997.

60 T. E. Kim, H. J. Jang, S. W. Park, J. Wei, S. Cho, W. I. Park, B. R. Lee, C. D. Yang and Y. K. Jung, *ACS Appl. Bio Mater.*, 2021, **4**, 3453.

61 S. Su, Y. Tian, Y. Li, Y. Ding, T. Ji, M. Wu, Y. Wu and G. Nie, *ACS Nano*, 2015, **9**, 1367–1378.